

## Chapter III.6

### Beam coupling impedance measurements with beam and on a bench

Nicolò Biancacci

CERN, Geneva, Switzerland

---

The beam coupling impedance is one of the key quantities describing the interaction between a particle beam travelling in a particle accelerator and its surroundings. Under specific circumstances, the impedance can lead to severe beam instabilities which limit the overall performance of a running accelerator or pose challenges for the achievement of a project.

In this contribution, we present the main techniques in use to characterize the impedance either with beam-based procedures, or with RF measurements on a test bench. The former is usually performed on running machines for which limitations are found or need to be assessed, the latter is typically performed before/after equipment installation and for validation purposes.

We will also introduce some of the measurement techniques used to characterize the electromagnetic properties of materials. This is relevant, for example, for the correct material modelling in simulations, or to validate a fabrication process.

---

The beam coupling impedance represents the electromagnetic interaction of a particle beam with the surrounding accelerator equipment (such as beam pipes, RF cavities, kickers, instrumentation, etc.) [1–3]. As the current flowing in the coils of the bending magnets creates the main magnetic field in the accelerator, in a similar way, a circulating beam represents a current source and, during the passage in accelerator equipment, excites electromagnetic (EM) fields. The EM fields created by a source particle can act back on the trailing particles in the beam. Given a trailing test charge at a distance  $s$  from the source, the change in momentum normalized to the source and test charges is called *wakefield*, or *wake function*.

For example, if we consider the longitudinal electric field  $\mathcal{E}_l$  created by a source charge with velocity  $v$ , charge  $Q$ , and longitudinal coordinate  $z_S = vt$ , this will induce a change in longitudinal momentum  $\Delta p_l$  on a test particle carrying the elementary charge  $q$  at  $z_T = z_S + s$  given by

$$\Delta p_l(s) = \int_{-\infty}^{\infty} dt q \mathcal{E}_l(z_T, z_S = vt) \Big|_{z_T = z_S + s}, \quad (\text{III.6.1})$$

where we neglected the possible dependence on the transverse coordinates of the source/test particles.

The longitudinal wakefield is defined as

$$W_l(s) = -\frac{v}{qQ} \Delta p_l(s). \quad (\text{III.6.2})$$

---

This chapter should be cited as: Beam coupling impedance measurements with beam and on a bench, N.Biancacci, DOI: [10.23730/CYRSP-2024-003.2029](https://doi.org/10.23730/CYRSP-2024-003.2029), in: Proceedings of the Joint Universities Accelerator School (JUAS): Courses and exercises, E. Métral (ed.),

CERN Yellow Reports: School Proceedings, CERN-2024-003, DOI: [10.23730/CYRSP-2024-003](https://doi.org/10.23730/CYRSP-2024-003), p. 2029.

© CERN, 2024. Published by CERN under the [Creative Commons Attribution 4.0 license](https://creativecommons.org/licenses/by/4.0/).

The frequency content of a wakefield created by a single particle is called *beam coupling impedance* or simply impedance.

Figure III.6.1 shows a schematic example of the concepts illustrated above. A charged particle beam excites the electromagnetic fields in a cavity (left). The normalized longitudinal momentum kick is given by the wakefield function (center), whose Fourier transform is the impedance definition (right).

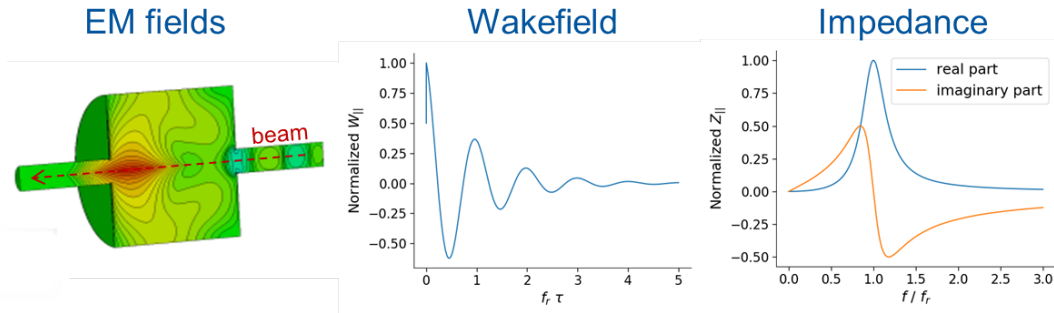


**Fig. III.6.1:** A charged particle beam excites electromagnetic fields in a cavity (left). The longitudinal wakefield and corresponding impedance are shown respectively in the center and in the right plots. Axes are normalized with respect to the main resonance frequency.

In analogous way, one could define the transverse wakefield and impedance. Depending on the plane and relative transverse source/test position we distinguish at least 5 impedances (and corresponding wakefields) as shown in Fig. III.6.2:

- the longitudinal impedance: both source and test particles are on-axis;
- the driving (or dipolar) impedance: the source particle is displaced transversally, whereas the test particle is on-axis;
- the detuning (or quadrupolar) impedance: the test particle is displaced transversally, whereas the source particle is on-axis.

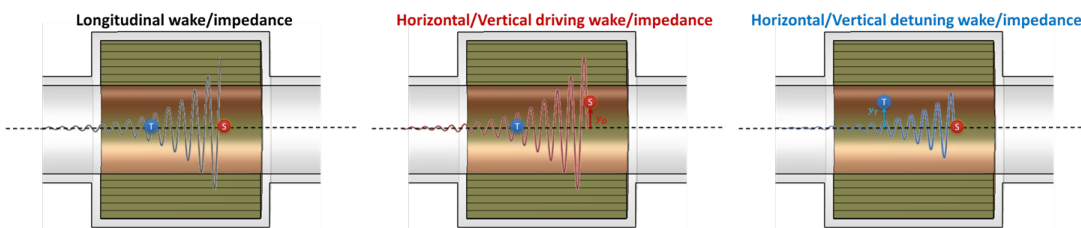


**Fig. III.6.2:** Five impedances (and corresponding wakefields) are needed for the development of an accelerator impedance model: the longitudinal (on the left), driving or dipolar (on the center), detuning or quadrupolar (on the right) impedances.

In principle, one could develop up to any order on source/test positions, but in practice the linear terms are usually sufficient for the development of an accelerator impedance model. It is important to notice that the concept of impedance reduces the problem of computing the scattered electromagnetic

fields in a structure from a beam excitation to a point charge excitation. Once the response (also referred to as *Green function*) is known, one can obtain the convoluted response from the full beam distribution.

The impedance is acting as a retro-action system on the beam response to self-excitation, similarly to what can happen putting a microphone in front of an amplifier speaker: the initial sound is indefinitely amplified as long as the output is seeding the input of the system. In the same way, the beam may undergo oscillations under the effect of the impedance, which self-enhance themselves inducing particle loss or beam quality degradation. Figure III.6.3 shows an impedance-driven instability recorded in the Large Hadron Collider (LHC).

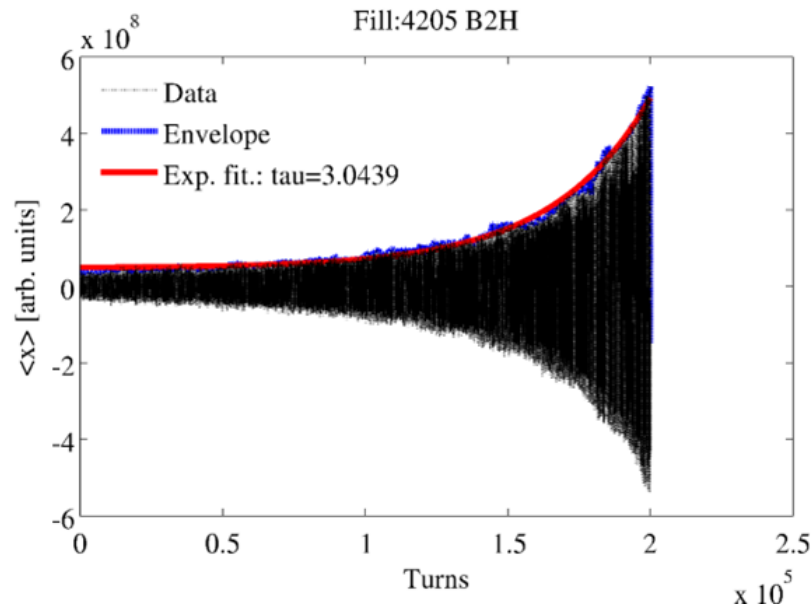


**Fig. III.6.3:** A coherent instability (i. e. from the centre of mass  $\langle x \rangle$ ) recorded in the horizontal plane of beam 2 during the LHC fill 4205.

By definition, the impedance is inherently present in every accelerator and it contributes to its intensity limitations, either directly or together with other collective effects (e.g. space charge, intrabeam scattering (IBS), electron cloud, beam-beam, etc.). Detrimental coherent and incoherent impedance driven effects can prevent the achievement of the final beam parameters (intensity, emittance, etc.) and it is therefore important to control, and in some cases necessary to reduce, the machine impedance.

In this context, the development of a machine impedance model allows to:

- predict the impedance-related machine performance limitations;
- prepare for machine upgrades (adding/removing impedances);
- optimize beam parameters for existing machine operation modes;
- be ready to address expected and unexpected instabilities.

Figure III.6.4 shows the typical result of the impedance model development for the LHC. For illustrative purpose, only the horizontal driving impedance is shown. The impedance is calculated, either analytically or with numerical simulations, for each machine element. As one can see, the largest

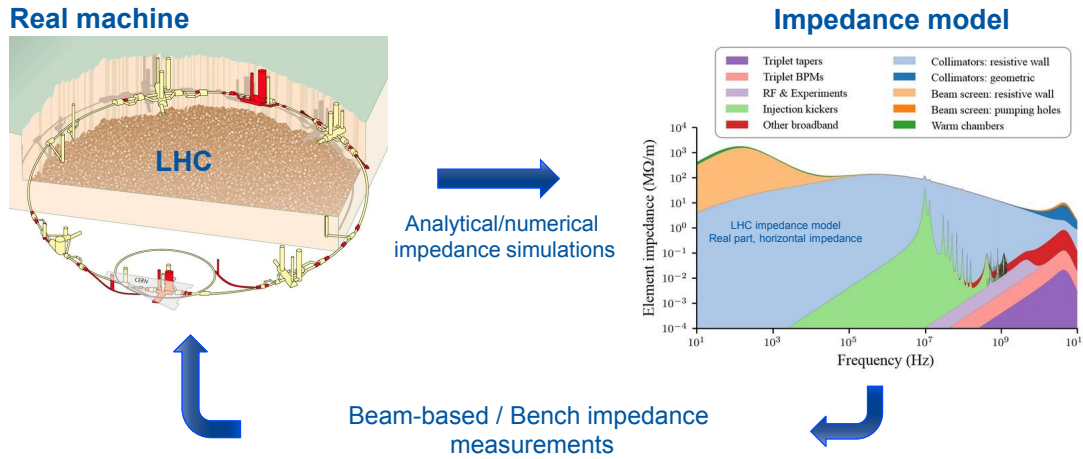


**Fig. III.6.4:** Example of an accelerator impedance model. On the left the LHC schematic is shown, on the right the corresponding model for the horizontal driving impedance. The quality of the model is strictly tested against beam-based or/and bench impedance measurements.

impedance contributors are typically the elements close to the beam (e.g. collimators) or/and large in number (e.g. the beam pipe). To ensure and test the quality of a model, the development of an impedance model is cross-checked and refined taking input from beam-based and bench impedance measurements.

### III.6.1 Beam-based impedance measurements

In this section we will describe some of the commonly performed beam-based impedance measurements. Figure III.6.5 shows a simplified (and not exhaustive!) list of the main techniques used to access the real and imaginary parts of the longitudinal and transverse impedances. The reader will contextually find appropriate references for a more detailed description of each technique.

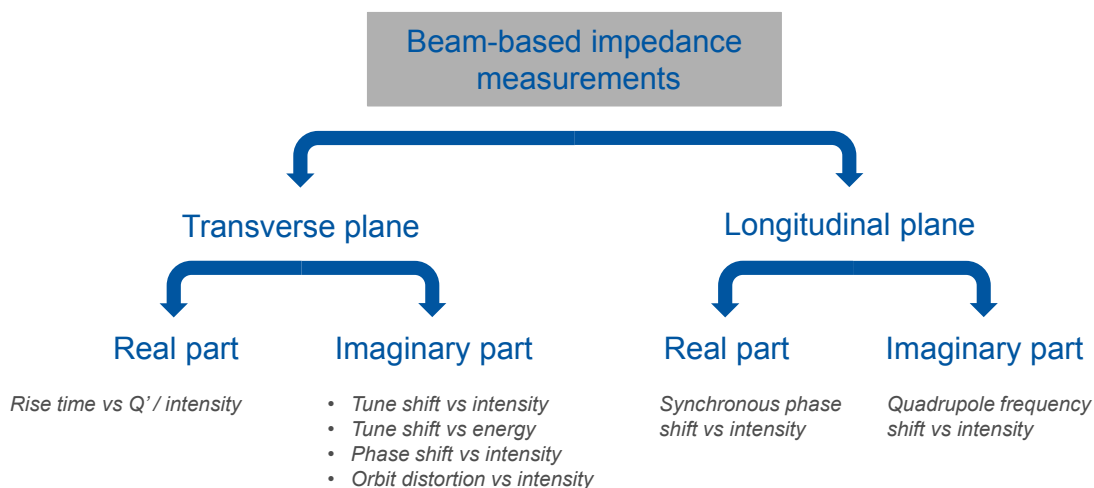


**Fig. III.6.5:** Schematic view of a selection of methods commonly used for beam-based impedance measurements in longitudinal and transverse planes.

### III.6.1.1 Transverse impedance

In absence of collective effects, the beam would undergo betatron oscillations along the closed-orbit path. This motion is described by Hill's equation

$$\frac{d}{ds}y_i(s) + K_0(s)y_i(s) = 0, \quad (\text{III.6.3})$$

in which  $K_0(s)$  represents the quadrupole magnet strength along the longitudinal coordinate  $s$ , and, to simplify the notation, we exclusively refer to the vertical coordinate  $y_i$  of a particle  $i$  in the beam. Applying a Floquet transformation we can find Hill's solution of Eq. (III.6.3) in the form

$$y_i(s) = \sqrt{\epsilon_y \beta_y(s)} \cos(\psi_y(s) + \theta_i), \quad (\text{III.6.4})$$

where  $\beta_y$  is the betatron function (or  $\beta$ -function) fixed by the lattice properties,  $\epsilon_y$  is the single particle invariant,  $\theta_i$  is the betatron phase at  $s = 0$  and  $\psi_y(s)$  the betatron phase advance along the lattice given by

$$\psi_y(s) = \int_0^s \frac{1}{\beta_y(s)} ds, \quad (\text{III.6.5})$$

where the integral starts from  $s = 0$ , a conventional accelerator starting point. We define the tune  $Q_y$  as the number of particle oscillations per turn given by

$$Q_y = \frac{1}{2\pi} \int_0^C \frac{1}{\beta_y(s)} ds, \quad (\text{III.6.6})$$

with  $C$  the accelerator circumference.

In presence of a transverse impedance, the motion is perturbed as

$$\frac{d}{ds}y_i(s) + K_0(s)y_i(s) = \frac{\langle F_i \rangle}{\beta^2 E_0}, \quad (\text{III.6.7})$$

where  $\langle F_i \rangle$  is the average force experienced by the particle,  $E_0 = \gamma m_p c^2$  is the energy of the travelling proton particle, with  $c$  the speed of light,  $m_p$  the rest mass,  $\gamma$  the Lorentz factor, and  $\beta = v/c$ .

Under these conditions, the centroid motion undergoes an exponential growth in amplitude with growth-rate  $\tau_y^{-1}$  directly proportional to the real part of the transverse impedance, and a betatron frequency shift, or tune shift  $\Delta Q_y$ , related to the imaginary part of the impedance.

This simplified picture purely refers to the rigid motion of the beam in presence of driving impedance. In reality the beam, as any physical structure, can have different modes of oscillations, each of them differently affected by the impedance. In this frame, codes like DELPHI [4] can provide a more detailed insight of the theory developed, e.g., in Ref. [2].

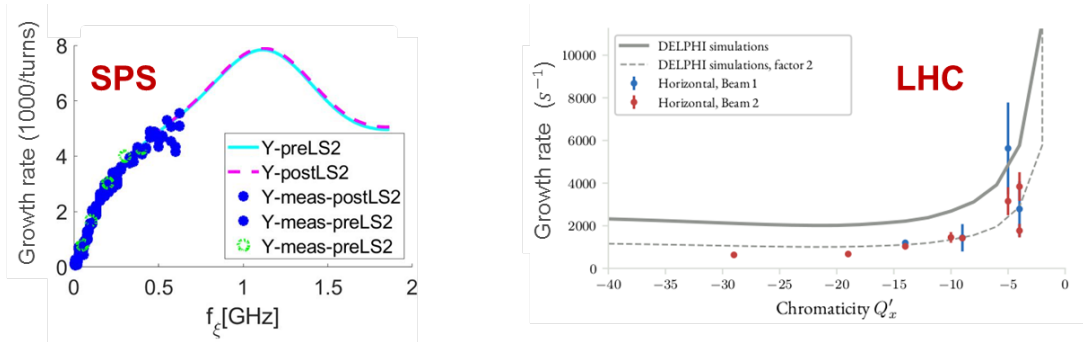
#### III.6.1.1.1 Real part

Figure III.6.3 showed an instability recorded in the LHC. The instability can be seen as an exponential growth of the centroid motion, eventually leading to particle loss on the beam pipe or collimation region of the machine. The rise time of the instability  $\tau_y$  (or, conversely, the growth-rate  $\tau_y^{-1}$ ) is directly related

to the real part of the transverse impedance: the larger the impedance, the shorter the rise time. In particular, looking at the dependence of  $\tau_y$  versus chromaticity  $Q'_y$ , one can deduce the behaviour of the real part of the machine impedance versus frequency. An example of the method application is shown in Fig. III.6.6 for the SPS [5] and for the LHC [6].

For the SPS, measurements are shown in dots, together with full or dashed lines representing the analytical estimations of the growth rate before/after the machine Long Shutdown 2 (LS2). Measurements are shown with respect to the chromatic frequency  $f_{\xi_y} = f_0 Q'_y / \eta$ , with  $f_0$  the beam revolution frequency and  $\eta$  the slippage factor. No change in the impedance was expected and confirmed by the measurements, which are in remarkable agreement with predictions.

For the LHC, measurements are shown in dots and tend to agree with the machine impedance model accounting for a factor of about 2 in the transverse impedance. This is an example where measurements help as an input for the refinement of the impedance model.



**Fig. III.6.6:** Determination of the real part of the transverse dipolar impedance in the SPS (left) and in the LHC (right). Courtesy of C. Zannini and D. Amorim respectively.

A beam undergoing oscillations with exponentially increasing amplitude will eventually hit the vacuum chamber and be lost. Rise-time measurements are therefore “easier” in fast-cycling machines, as one can inject new bunches rapidly. In large colliders, like the LHC, a machine refill can take hours, especially for experiments at high energy. In this case, the technique can be still used with the help of a transverse damper: once the instability is triggered, the damper gain is quickly increased in order to damp it. If the beam parameters (e.g. emittance, intensity) have not been degraded, one can “re-use” the beam for another measurement.

### III.6.1.1.2 Imaginary part

The tune shift  $\Delta Q_y$  is proportional to the imaginary part of the transverse impedance at a given intensity. The behaviour versus intensity is typically linear in the low-intensity regime, and one can deduce the net contribution of the machine impedance by studying the linear tune shift versus intensity.

The procedure is illustrated in Fig. III.6.7: the beam is kicked by a transverse kicker and the centroid motion recorded at one beam position monitor (BPM) in the machine. On the right plot, the tune variation versus intensity in the PS at injection energy is shown, from which one can deduce a total machine (imaginary) impedance of about  $9 \text{ M}\Omega/\text{m}$  [7]. In this particular case, where the machine is

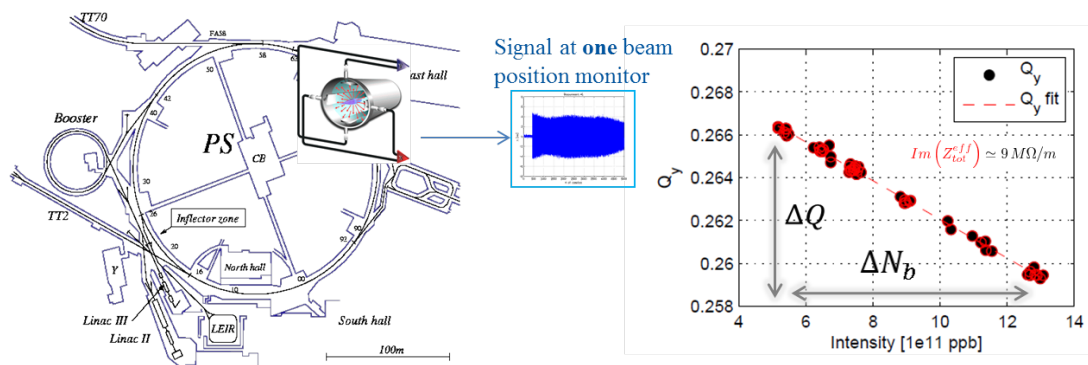


**Fig. III.6.7:** Tune shift versus intensity measurements in the PS in the vertical plane.

tuned at low chromaticity and the beam is kicked, the transverse impedance represents the summation of driving and detuning impedances.

An other interesting case is shown in Fig. III.6.8 for the SPS [8]. On the left plot, the tune variation versus intensity on the horizontal plane is shown to be negligible: this is due to the cancellation between the transverse driving and detuning impedances, which are equal but of opposite sign due to the flat shape of the SPS beam pipe. On the right plot, one can appreciate how, adding more elements into the machine impedance model, one can approach the measured tune shift in the vertical plane.

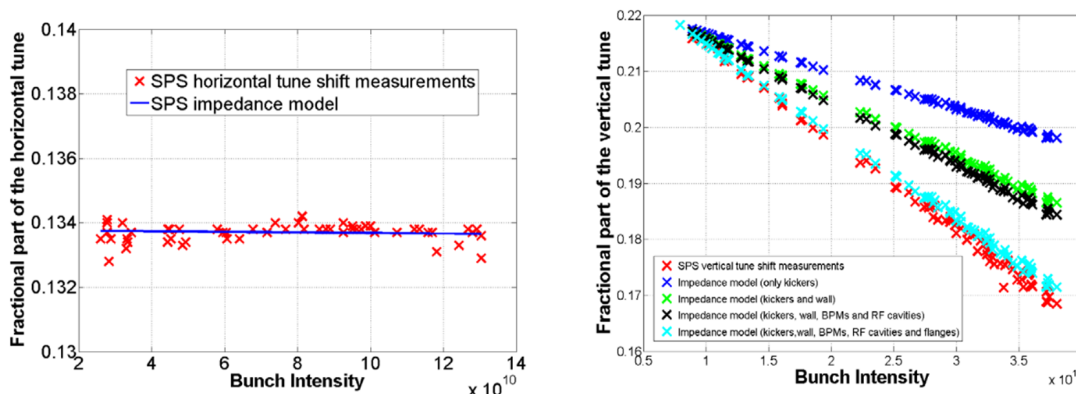


**Fig. III.6.8:** Tune shift versus intensity measurements in the SPS. On the left the horizontal plane, on the right the vertical one. Courtesy of C. Zannini.

The tune shift measured in low-energy machines exhibits a large contribution related to the indirect space charge (ISC). It is often desired to precisely know the fraction of impedance related to the machine equipment itself, removing the contribution of the indirect space charge. Measuring the transverse impedance versus intensity at various energies allows to disentangle the role of the energy-dependent contribution of the impedance. Figure III.6.9 reports an example of the measurement performed in the PS where the expected dependence  $Z_y^{ISC} \propto 1/\beta\gamma^2$  is shown [9].

Measuring the tune shift versus intensity gives information on the total machine impedance of an accelerator, which is necessary to build a reliable impedance model. Nevertheless, the element-by-element contribution is sometimes desirable, especially if a strong impedance source is suspected. This

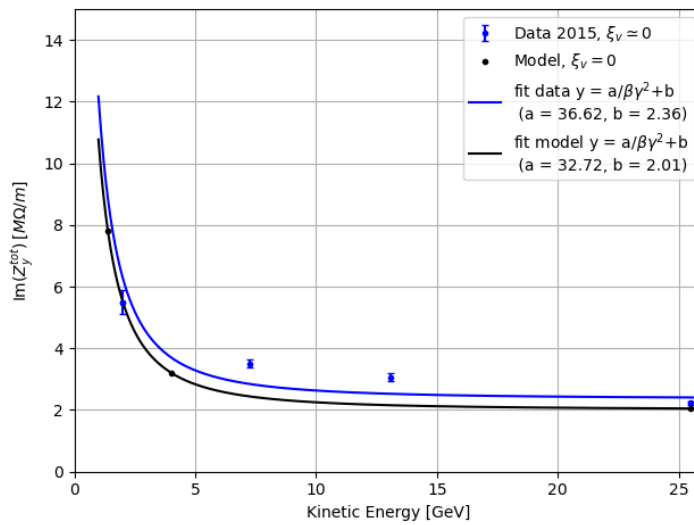


**Fig. III.6.9:** Energy dependent impedance measurement in the PS.

is why a number of impedance localization techniques have been developed over the years [10], using, for example:

1. the variation of phase advance vs. intensity;
2. local orbit bumps around specific devices;
3. physically movable devices (as collimators).

1) *Variation of phase advance vs intensity*

As the tune shift convolutes the information of the full accelerator, the phase-advance shift versus intensity gives information on the localized impedance between two BPMs. Figure III.6.10 shows a simulation of the effect of a strong impedance source in the PS: the phase-advance beating exhibits a kink at the source location, analogously to the beating induced by a thin quadrupole error.

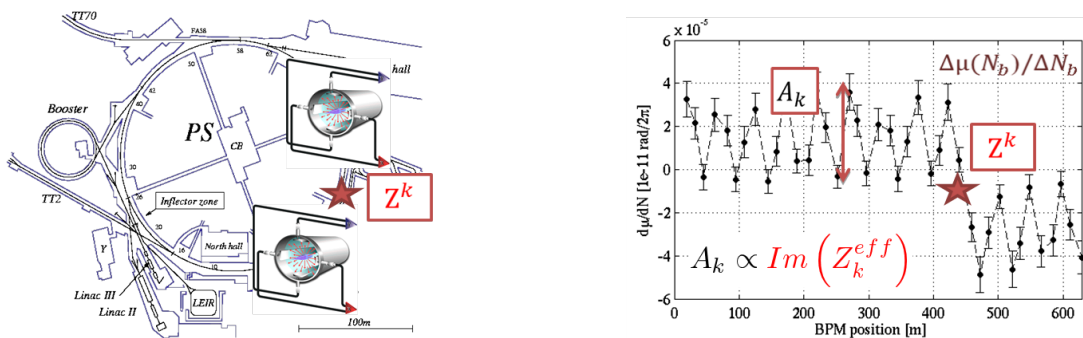


**Fig. III.6.10:** Simulation of the effect of a strong impedance source in the PS. The beating wave exhibits a kink at the source location.

It is therefore possible to reconstruct the impedance location with a least-squares minimization procedure, accounting for the possible impedance locations in the machine and their response in terms of

phase-advance beating [11]. The result of this procedure is shown in Fig. III.6.11 for the PS at 26 GeV. At the bottom the phase-advance shift recorded by the BPMs is shown in black, together with the least-squares reconstruction in red. At the top the strength of possible impedance sources is shown in terms of fraction of the total machine tune shift. It is interesting to notice that the kickers in section 71 exhibit the highest impedance contribution of the machine, in line with Ref. [7].

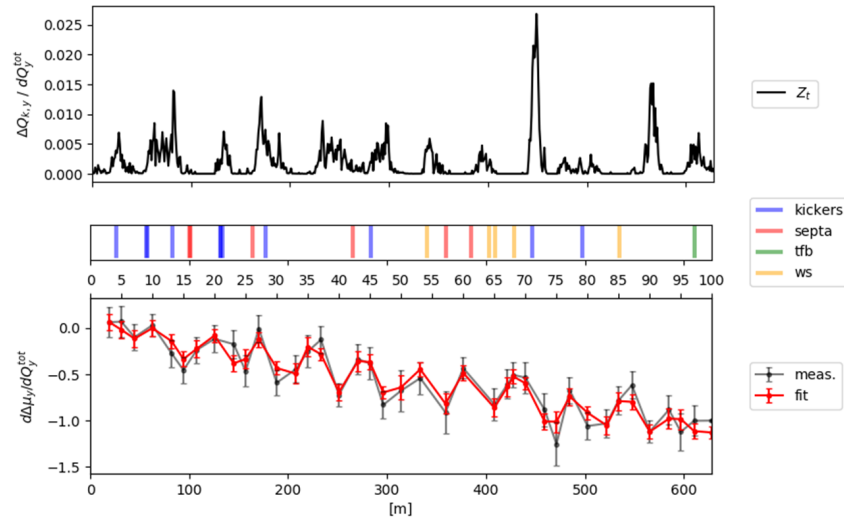


**Fig. III.6.11:** Measurement and reconstruction of the phase-advance shift versus intensity (at the bottom) and impedance sources along the 100 corresponding sections of the ring (at the top) in the PS at 26 GeV.

## 2) Local orbit response around specific devices

Another way to measure impedances in localized sections of the machine is by applying orbit bumps and recording the closed-orbit distortion at various intensities. The impedance kick in a ring location is proportional to the beam-orbit displacement. Therefore, scanning the local orbit-bump amplitude we can probe the device transverse impedance. Figure III.6.12 shows two examples of the procedure applied in the APS [12] and NSLS-II [13] machines.

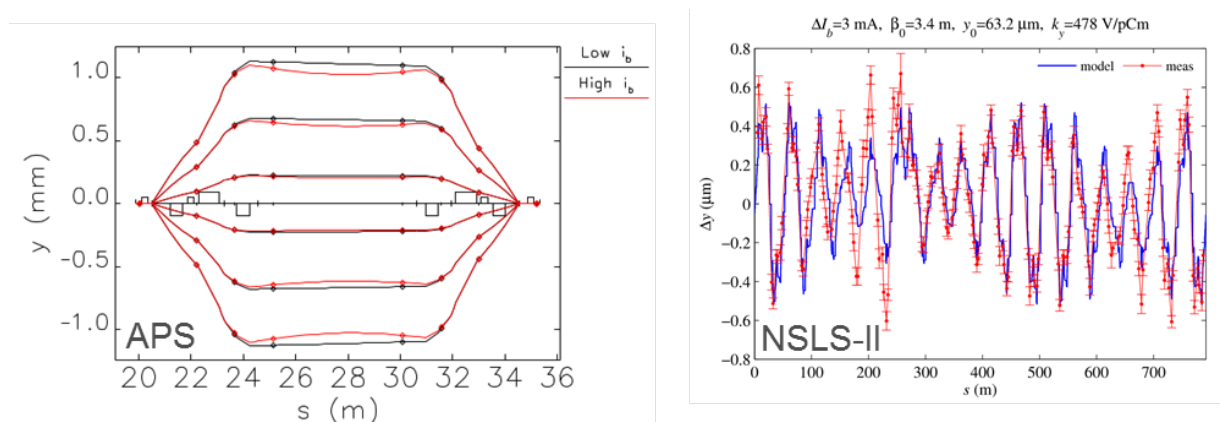


**Fig. III.6.12:** Orbit distortion due to a localized impedance source with orbit bumps in the ALS (left) and NSLS-II (right). Courtesy of L. Emery and V. Smaluk respectively.

3) *Physically movable devices*

Certain devices, typically insertion ones, can change their relative position with respect to the beam-orbit, therefore changing the impedance seen by the beam. We will consider the specific case of collimators. These are typically made of two parallel jaws of absorbing material and are installed to clear the beam halo and protect the machine from uncontrolled beam losses. Due to the proximity to the beam and their large number, collimators often share a large fraction of the total machine impedance. The transverse impedance of a collimator, in the collimation plane, is given by (in the classical thick-wall regime)

$$Z_y \propto \sqrt{\rho}/b^3, \quad (\text{III.6.8})$$

where  $\rho$  is the jaw resistivity and  $b$  the collimator gap. Given this relation, measuring the tune-shift variation versus gap can give information about the device resistivity. This experiment was relevant, for example, at the design stage of the low impedance collimators of the High-Luminosity LHC (HL-LHC), when different jaw material choices were under discussion. Figure III.6.13 shows, on the right, a section of a tested collimator with three different stripes of materials exposed to the beam: TiN, MoGr and Mo. These material choices have lower resistivity with respect to the formerly installed LHC collimators, made in Carbon Fiber Composite (CFC,  $\rho = 5 \mu\Omega\text{m}$ ). On the left, the tune shift versus gap is shown, confirming the reduced impedance in correspondence to the Mo stripe [14].

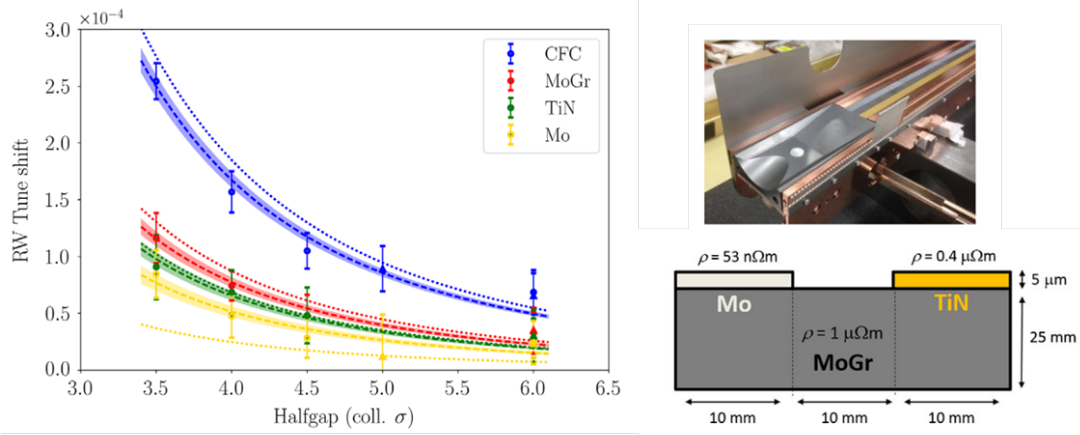


**Fig. III.6.13:** On the left, tune shift versus gap corresponding to four different materials seen by the beam in the LHC. On the right, section of the 3-stripes collimator prototype for material testing (top) and details of the jaw cross-section (bottom).

### III.6.1.2 Longitudinal impedance

#### III.6.1.2.1 Real part

Under the effect of the longitudinal impedance  $Z_l$ , the beam loses energy which needs to be supplied back by the RF cavities. The energy loss  $\Delta E$  is given by Ref. [2]

$$\Delta E = \frac{q^2 N_p}{T_0} \sum_p \text{Re}[Z_l(p\omega_0)] \lambda^2(p\omega_0), \quad (\text{III.6.9})$$

where  $N_p$  is the number of particles in the bunch,  $T_0$  the revolution period,  $\lambda^2(p\omega_0)$  the power spectrum of the bunch distribution sampled at the  $p^{\text{th}}$  revolution harmonic. The energy loss is recovered by a (synchronous) phase shift  $\Delta\varphi$  given by

$$\Delta E = qV_{\text{RF}} \cos(\varphi_{s,0})\Delta\varphi, \quad (\text{III.6.10})$$

where  $V_{\text{RF}}$  is the RF voltage of the main cavities operating at the unperturbed synchronous phase  $\varphi_{s,0}$ . Measuring the variation of the synchronous phase shift versus intensity gives information on the real part of the longitudinal impedance convoluted by the beam spectrum. This is shown for example in Fig. III.6.14, where the time (phase) delay between a low intensity bunch (probe) and a bunch with variable high intensity is recorded in the PS. The linear fit provides the real part of the machine impedance [15].

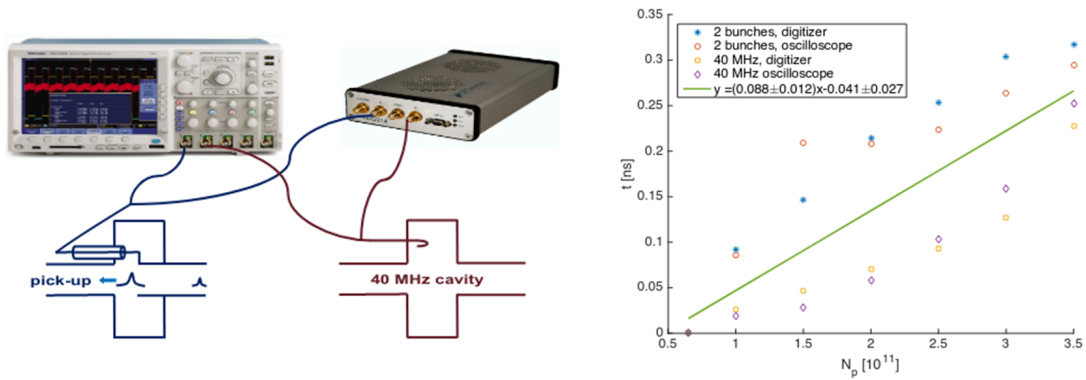


**Fig. III.6.14:** On the left, sketch of the phase-shift measurement setup used to probe the time distance between a high- and low-intensity bunch with respect to the 40 MHz reference cavity in the PS. On the right, the time delay recorded as a function of intensity.

### III.6.1.2.2 Imaginary part

Bunch-length oscillations, corresponding to the longitudinal quadrupole mode, can be effectively used to measure the imaginary part of the longitudinal impedance. The dependence of the oscillation frequency on the intensity is related to the convolution of the reactive part of the impedance with the bunch spectrum [16].

An example from the SPS is given in Fig. III.6.15. Bunches with different intensities and bunch lengths are injected in the machine. The mismatch to the RF bucket provokes strong quadrupole oscillations whose frequency is recorded. The linear dependence as a function of the intensity is related to the reactive part of the impedance. Varying the bunch length provides information on the frequency dependence of the longitudinal impedance [17].

### III.6.1.3 Other methods

The classification presented and shown in Fig. III.6.5, as already commented, is not exhaustive. Other methods can be used depending on the specific beam and machine parameter configurations, as well as on the level of accuracy up to which the impedance model needs to be developed. It is nevertheless

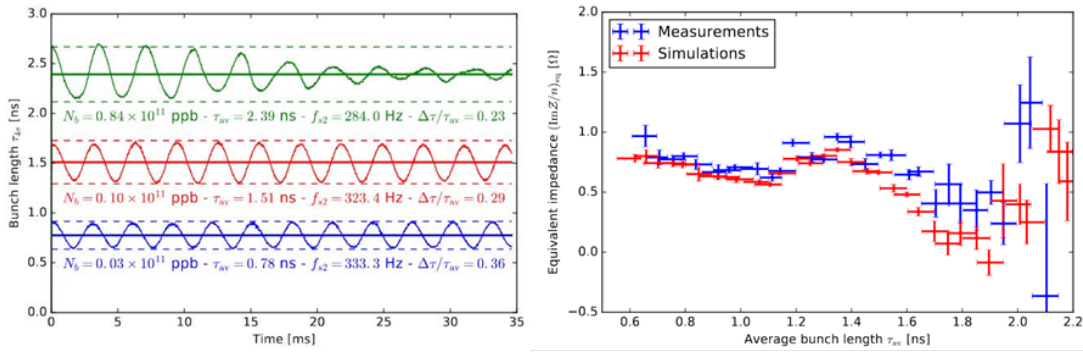


**Fig. III.6.15:** On the left, bunch-length oscillations for bunches of different average bunch lengths injected in the SPS. On the right, effective reactive impedance as a function of the average bunch length. Courtesy of A. Lasheen.

important to cite those methods based on the use of an active excitation of the beam with a transverse damper, allowing not only to deduce the machine impedance, but also the threshold for the loss of Landau damping (see e.g. Ref. [18]). In the frame of impedance localization, an AC-dipole driven excitation can be used as an accurate measurement tool [19]. Other non-destructive methods are based on the analysis of the beam transfer function and on the measurement of the Schottky spectrum [20]. The latter is particularly common for machines running coasting beams such as LEIR [21].

#### III.6.1.4 Synergy between different methods: the LHC TDI

The methods shown until now provide different observation points on a common subject, the determination of the impedance of a machine. It is therefore natural that the synergy of different methods can provide better and more comprehensive knowledge than the application of a single technique.

An example comes from the LHC TDI. The TDI (Target Dump Injection) is a special device installed in the LHC aiming at protecting the machine from injection failures [22]. There is one device per beam: TDI2 (for beam 1) and TDI8 (for beam 2). The absorbing blocks should sustain the impact of a full LHC beam and the jaw was originally designed as a series of Ti-coated hBN (hexagonal boron nitride) blocks, Al coated with NEG (non-evaporable getter) and CuBe (copper beryllium) materials.

In 2015 an anomalous behaviour was observed during operation (excessive vacuum spikes) and correlated to the TDI8 movement. Beam-based measurements were performed on the two LHC beams in order to access the longitudinal and transverse impedance of the machine. Figure III.6.16 shows the result of the synchronous phase-shift measurements, on the left, and of the tune-shift measurements, on the right. From both measurements, a significantly larger impedance was recorded for TDI8 with respect to TDI2, confirming that the machine issue was indeed impedance-related. In particular, the synchronous phase shift of TDI8 was found to be a factor of about 2 larger than the one of TDI2. Similarly, the tune shift was about 4 times larger than the one of TDI2.

Once removed from the machine, detailed bench-impedance measurements were performed on the devices (see Sections III.6.2.1 and III.6.2.2 for details), which indeed confirmed the degradation of TDI8 with respect to TDI2.

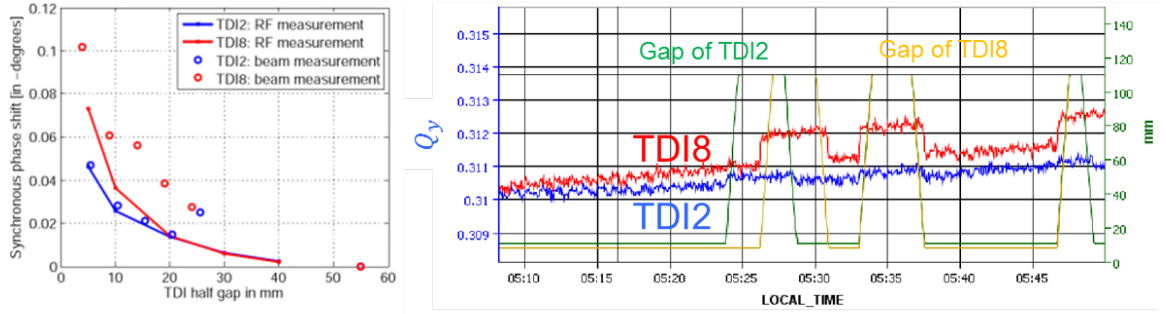


**Fig. III.6.16:** Beam-based impedance measurements on the LHC TDIs in 2015. On the left, measurement of the synchronous phase shift versus TDI aperture, on the right, measured tune-shift variation while changing the TDI gap. Courtesy of J. F. E. Müller and B. Salvant respectively.

### III.6.2 Bench impedance measurements

The impedance of a device can also be measured directly on a test bench. This is typically performed during the production campaign of new equipment for impedance validation purposes. In other cases, equipment from running machines may require bench impedance measurements when non-conformities and anomalies are detected during machine operation (e.g., excessive heating, pressure rise or spikes, etc.). Several methods, mainly based on RF techniques, can be used and compared to numerical simulations. In this section we will cover the following techniques:

- Stretched-wire method;
- Resonant-wire method;
- Resonant-mode characterization.

Additional information and techniques can be found in Ref. [23].

#### III.6.2.1 Stretched-wire method

A beam travelling into an accelerator device can be seen, in the ultra-relativistic limit, as a source current exciting a perfectly planar electromagnetic field given by

$$\mathcal{E}_r = Z_0 \mathcal{H}_\varphi = Z_0 \frac{q}{2\pi r} e^{-j\omega \frac{z}{c}}, \quad (\text{III.6.11})$$

where  $\mathcal{E}_r$  and  $\mathcal{H}_\varphi$  respectively represent radial electric and azimuthal magnetic fields and  $Z_0$  is the characteristic impedance of vacuum. This field is qualitatively similar to that of a coaxial transmission line. This is why a wire stretched along a device and carrying a current pulse can be used to measure the beam coupling impedance of the device itself [24]. The main drawback of this technique is the introduction of an additional inner conductor (the wire), which eventually changes the electromagnetic boundaries and introduces energy loss already below the beam pipe cut-off [25]. Nevertheless, being a very practical solution, it is often used in the accelerator community. Moreover, the result can nowadays be directly compared to a simulated stretched-wire setup.

The wire can be considered the continuation of the inner conductor of the coaxial cables used for RF measurements. In this context, the measurement of the beam coupling impedance can be performed with a Vector Network Analyzer (VNA) measuring the transmission and reflection scattering parameters of the device under test (DUT).

If the lumped-element approximation holds (DUT length  $L_{\text{DUT}} \ll \lambda$ , with  $\lambda$  the wavelength at the highest frequency of interest) we can calculate the impedance from the transmission scattering parameters of a series element. The relation between the longitudinal beam coupling impedance  $Z_l$  and the scattering parameters is given in this case by the Hahn-Pedersen formula [26]

$$Z_{\text{HP}} = 2Z_c \frac{S_{21}^{\text{ref}} - S_{21}^{\text{DUT}}}{S_{21}^{\text{DUT}}}, \quad (\text{III.6.12})$$

where  $Z_c$  is the characteristic impedance of the transmission line created by the wire and the DUT,  $S_{21}^{\text{ref}}$  is the transmission scattering parameter in absence of the DUT (e.g. an ideal beam pipe) and  $S_{21}^{\text{DUT}}$  the transmission scattering parameter measured on the DUT.

For electrically long devices, and  $Z_l \simeq Z_c$ , the lumped-impedance formula is not accurate and the so called log-formula can be used [27]. This is given by

$$Z_{\text{log}} = -2Z_c \log \left( \frac{S_{21}^{\text{DUT}}}{S_{21}^{\text{ref}}} \right), \quad (\text{III.6.13})$$

where  $\log$  is the natural logarithm. Additional refinements have been proposed over time. For example, in case of large distributed impedances the *improved* log-formula can be used [28].

The DUT characteristic impedance needs to be matched to that of the cables connecting source and load (typically 50  $\Omega$ ). Bi-directional matching is achievable with a series and a parallel resistor. More practically, only the internal matching is implemented (waves in the DUT back to the source/load) with a series resistor as shown in Fig. III.6.17. External matching (waves from source/load back to the DUT) can be improved with additional attenuators [29].

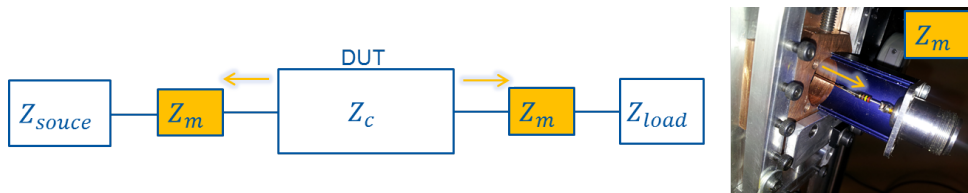


**Fig. III.6.17:** On the left, schematic view of DUT connected to a source and a load through cables and matching network  $Z_m$ . On the right, a matching network made with a series resistor in a sucobox.

The value of  $Z_c$  can be computed analytically for an air-filled coaxial line structure as

$$Z_c = 60 \log \left( F \frac{d_{\text{max}}}{d_{\text{min}}} \right), \quad (\text{III.6.14})$$

where  $F$  is a form factor depending on the outer conductor geometry ( $F = 1$  for a cylindrical line, and  $F = 1.27$  for parallel plates),  $d_{\text{max}}$  is the largest dimension of the DUT seen by the wire,  $d_{\text{min}}$  is the

diameter of the wire.

More accurately,  $Z_c$  can be found with the Time Domain Reflectometry (TDR) technique, i.e. converting the  $S_{11}$  and  $S_{22}$  parameters into input impedance (without matching resistors and attenuators). Applying a Fourier transformation, one can inspect the impedance along the device length. This operation is automatically performed by VNAs. Figure III.6.18 shows an example of a TDR measurement of an LHC collimator: the characteristic impedance is shown along the DUT length and increases with the collimator gap as expected for a coaxial line structure [30].

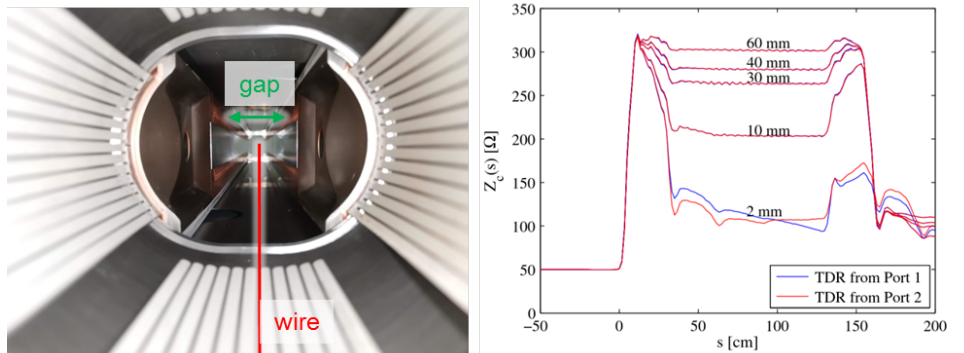


**Fig. III.6.18:** On the left, front view of a collimator. On the right, TDR measurement of the characteristic impedance of the collimator versus gap.

The stretched-wire method was applied to the LHC TDI's in 2015, following the anomalous behaviour observed in operation and the results of dedicated beam measurements (see Section III.6.1.4). Figure III.6.19 shows the longitudinal impedance of TDI2, on the left, and TDI8, on the right: the measurement confirms the larger impedance of TDI8 with respect to TDI2, in particular when the wire approached the jaw surface. Surface inspection confirmed, lately, that part of the Ti coating on hBN volatilized and this event triggered a general review of the device's jaw absorber materials [31].

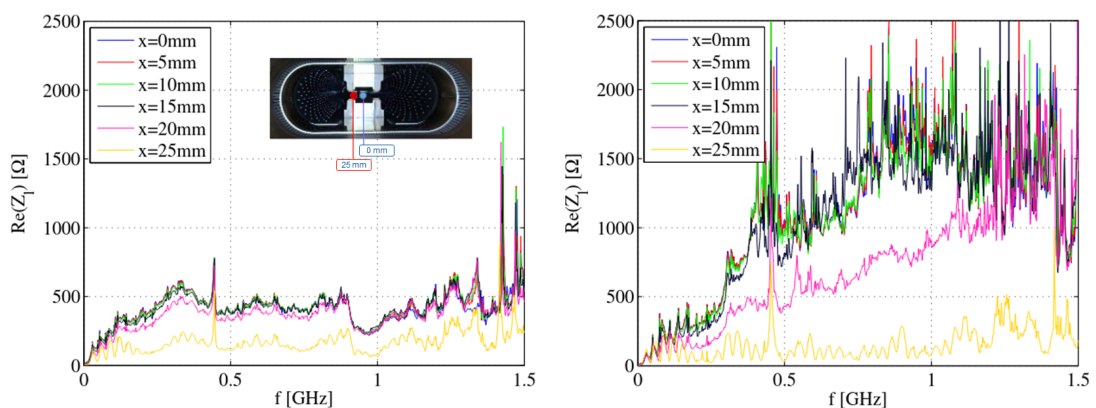


**Fig. III.6.19:** Stretched-wire measurements on TDI2, on the left, and on TDI8, on the right, as a function of wire horizontal position. For  $x = 0$  the wire is the middle of the jaws.

III.6.2.2 Resonant-wire method

When a small impedance needs to be measured, or the device is difficult (or impossible!) to match, the resonant-wire method can be used replacing the matching resistor with a weakly-coupled matching capacitor [32]. A small capacitance (order of few pF) can be easily produced approaching two wires as shown in Fig. III.6.20.

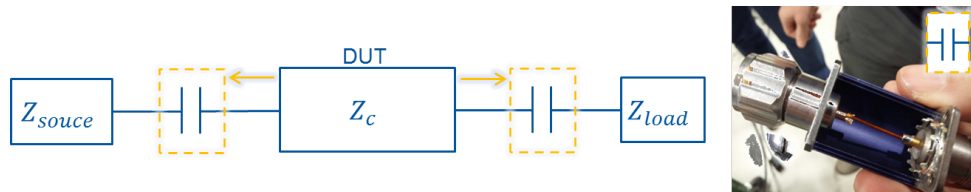


Fig. III.6.20: On the left, schematic view of a DUT connected to a source and a load through cables and matching capacitors. On the right, a matching capacitor made by approaching two wire segments in a sucobox.

The DUT is transformed into a transmission line resonator. A series of resonances occurs when  $L_{DUT} = n\lambda/2$  with  $n \in \mathbb{N}$ . From the quality factor  $Q_0$  of the resonances one can deduce the real part of the impedance, while, from the frequency shift with respect to an ideal delay line, one can obtain the imaginary part.

At resonance the matching is perfect. With respect to the classic stretched-wire method, one buys precision at the price of frequency resolution. The method is ideal for low impedances, as very large ones would lead to low quality factor and resonances might overlap.

As an example we show here resonant-wire measurements performed on the TDI and compared to the classic stretched-wire method. As one can see from Fig. III.6.21, the resonant-wire measurements are well in line with the classic stretched-wire ones for both TDI2 and TDI8. One can also observe that the wiggle at low frequency is absent when using matching capacitors. Nevertheless one cannot measure too large impedances as shown for the case of TDI8 at the smallest gap.

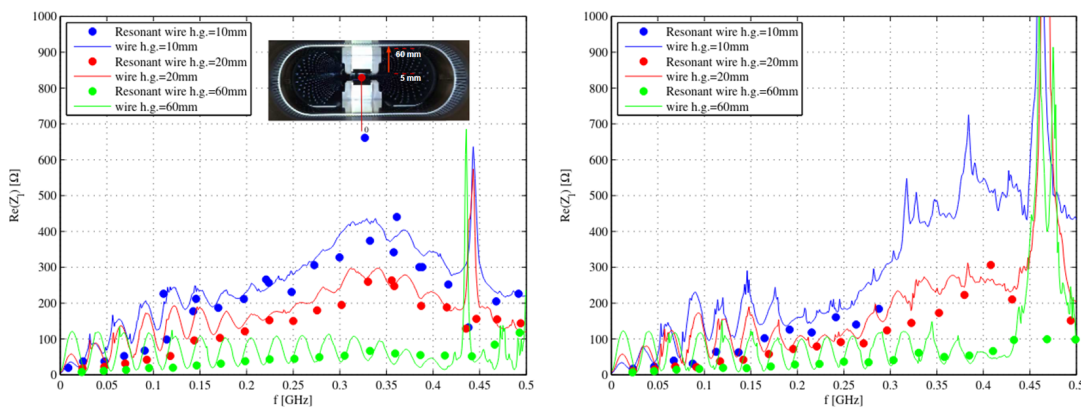


Fig. III.6.21: Resonant measurements performed on TDI2 and TDI8 as a function of the collimator gap and for different apertures.

### III.6.2.3 Resonant-mode characterization

Accelerator structures can exhibit resonant modes potentially harmful to the beam. A resonator impedance is fully characterized by the shunt impedance  $R_{sh}$ , the resonant frequency  $f_r$  and the quality factor  $Q_0$  with the expression

$$Z_l(f) = \frac{R_{sh}}{1 + jQ_0(f/f_r - f_r/f)}. \quad (\text{III.6.15})$$

Wire measurements are generally not suitable for resonant-mode characterization due to the introduction of power loss associated to the TEM-mode propagation [25]. Nevertheless, if the mode is weakly coupled results have been found quite reasonable [30].

As an alternative approach, probes can be used to characterize  $f_r$  and  $Q_0$  of the modes, while  $R_{sh}$  can be obtained with perturbation methods such as the bead-pull [33].

Inserting a probe into the DUT we can couple to the electric or magnetic field of a resonant mode. The termination part can be modified in order to test different coupling mechanisms: one can use a straight or bent probe, or a loop termination as shown in Fig. III.6.22 on the left. The probe ensures a good coupling to the electric field of possible resonant modes while the loop couples mainly to the magnetic field. The right side of Fig. III.6.22 shows a case in which low frequency modes were better coupled magnetically (i.e. with a loop) than electrically [30]. Once resonant modes have been characterized, appropriate measures might be necessary to reduce their impact on beam stability (e.g. ferrites were used in [30] to damp potentially harmful low frequency modes).

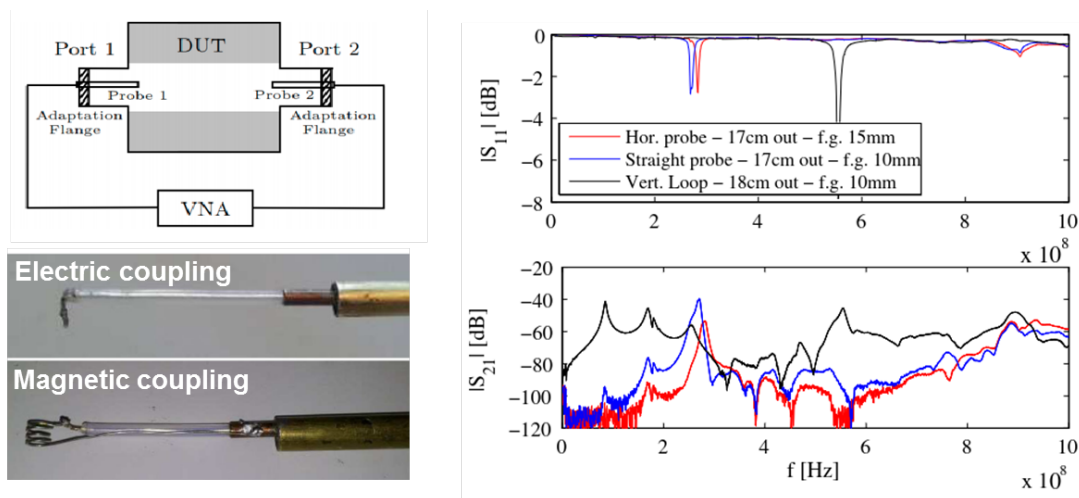


**Fig. III.6.22:** On the left, schematic of probe measurements in transmission (top) and examples of electric and magnetic couplers (bottom). On the right, resonant measurements performed on an LHC collimator with straight/bent probe and a loop.

### III.6.3 Materials characterization

The knowledge of accurate material properties is essential to correctly model the material impact on the impedance evaluation, especially when performing numerical simulations. From the electromagnetic point of view, we will address here the measurement of conductivity, permittivity and permeability.

We do not aim to a comprehensive description, but present several techniques designed around specific conditions (like beam frequency spectrum, machine operating temperature, bias magnetic field, etc.).

### III.6.3.1 Measurement of conductivity

Let us consider, firstly, the classic case of measurement of conductivity in DC. The most basic technique consists in the application of Ohm's law  $V = RI$  with  $R$  the resistance to be determined,  $I$  the applied current, and  $V$  the voltage drop [34]. Plugging two electrodes of an ammeter across a resistor would allow to measure it. Nevertheless some pitfalls exist: the electrodes introduce a contact resistance  $R_c$ , therefore the measured quantity would be  $R + 2R_c$ . This is particularly relevant when measuring a low resistance. This limitation can be overcome by the four-point (or four-probe) method, in which the current is measured at the sample extremities with an ammeter, and the voltage drop across the inner part of the sample with a voltmeter as shown in Fig. III.6.23. The voltmeter, having high impedance, will allow minimal current flow, i.e. voltage drop, on the contacts.

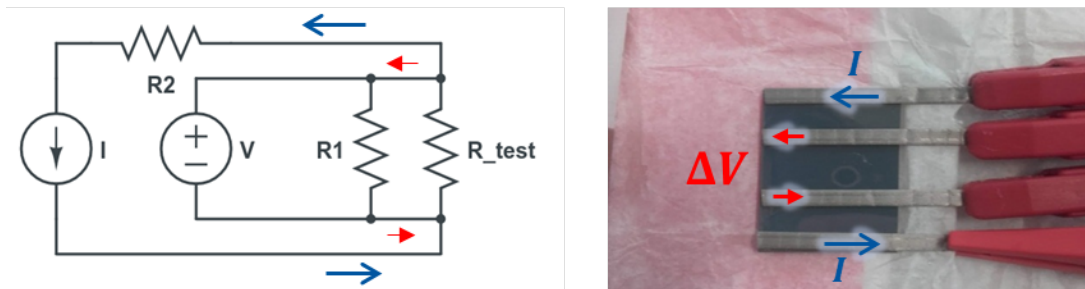


**Fig. III.6.23:** On the left, schematic of the four-point method: an ammeter is connected in series to a resistor, the voltmeter in parallel. On the right, the method application to measure a coated sample. In this case the method is also referred as “four-wire”.

From DC to few MHz, one can apply standard Non-Destructive Testing methods (NDT) such as Eddy-Current Testing (ECT). The simplest one, also implemented in commercial sigmeters, is based on the impedance response of a coil placed nearby a conductive substrate [35, 36].

The principle of the eddy-current technique is based on the interaction between a magnetic field source and a test material. When an alternating current flows through a coil, it generates a primary electromagnetic field. For frequencies below the self-resonance of the coil, the coil can be seen as an inductor generating a primary magnetic field. When the field is approached by an electrically conductive material, the primary magnetic field induces eddy currents which generate in turn a secondary magnetic field as shown schematically in Fig. III.6.24 at the top. As a result, the coil input impedance  $Z_{coil}$ , typically measured with an LCR-meter, will change by an amount  $\Delta Z_{coil}$  according to the electromagnetic properties of the material under test. Depending on the material, one can correlate the change in coil input impedance to the material resistivity.

The technique typically requires the sample thickness  $t_{bulk}$  to be at least  $3 \delta_{skin}$ , where  $\delta_{skin}$  is the skin depth at the operating frequency  $f$  defined as

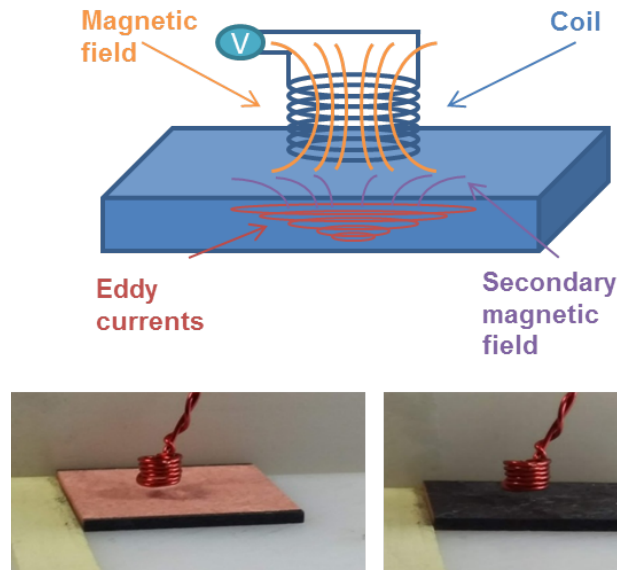


**Fig. III.6.24:** At the top, schematic view of the ECT: the primary magnetic field induces eddy currents which generate in turn a secondary magnetic field. At the bottom, on the left, a thin copper coating is measured, while on the right a MoGr bulk sample.

$$\delta_{\text{skin}} = \sqrt{\frac{\rho}{\pi\mu_0 f}}, \quad (\text{III.6.16})$$

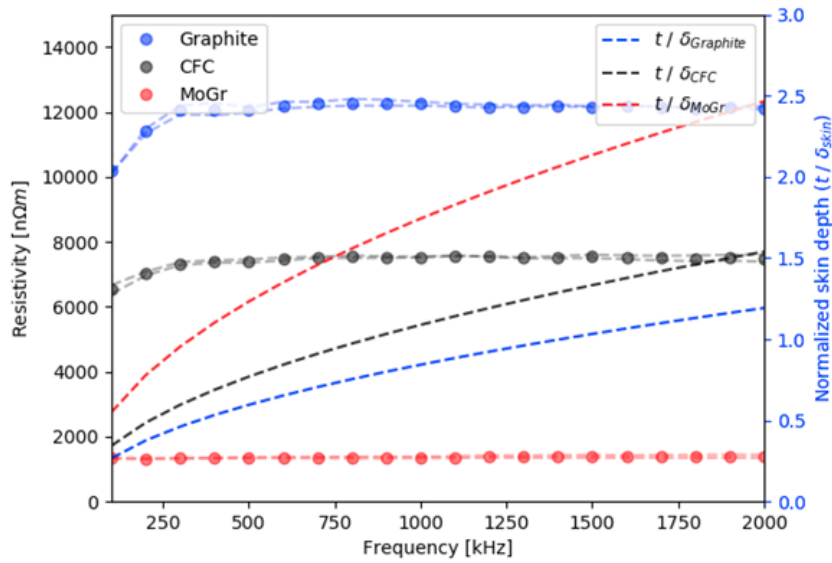
with  $\mu_0$  the vacuum permeability.

Figure III.6.24 (bottom), shows also an in-house implementation of the method setup for the characterization of thin resistive coatings at CERN [37]. On the left, a thin copper coating is measured, typically 5  $\mu\text{m}$  thick, on the right a MoGr bulk sample.

An example of measurement result is reported in Fig. III.6.25, where the measured resistivity for CFC, graphite and MoGr samples versus frequency are shown. It is interesting to notice that the resistivity of graphite and CFC samples, despite the large penetration depth in the material, can be obtained already for  $t_{\text{bulk}}/\delta_{\text{skin}} \simeq 0.5$ .

At higher frequencies, typically GHz, a cylindrical resonator operating in the H011 mode could be used as an alternative method to the ECT [38]. Given the high operation frequency, thin samples, such as coatings, can be easily tested. The basic principle is to leave one side of the resonator open so that different samples can be measured. From the variation of the H011 mode  $Q_0$ , one can deduce the resistivity of the tested material. The choice of the H011 mode (or any H01n mode) is dictated by the absence of current flows on the end cap extremities of the cavity, as shown in Fig. III.6.26 on the right. The cavity dimensions are a compromise between the practical manufacturing and the high frequency of operation needed to have the skin depth smaller than the material thickness.

The left side of Fig. III.6.26 shows a manufactured cavity connected to the VNA excitation ports in which tiny loops couple to the magnetic field of the H011 mode. The end cap can be replaced by different material samples, either for calibration or measurement purposes.



**Fig. III.6.25:** Measured resistivity for CFC, graphite and MoGr samples as a function of frequency (dotted lines) together with sample thickness normalized to the material penetration depth (dashed lines).



**Fig. III.6.26:** On the left, fabricated cylindrical resonator with removable end cap. On the right, H011 mode magnetic and electric field lines in a cylindrical cavity. No current flow is present on the contact surface.

The method was applied for systematic measurements of Mo-coated MoGr samples at CERN in the frame of the production of low-impedance collimators for the HL-LHC [37]. As shown in Eq. (III.6.8), the lower the jaw resistivity, the lower the impedance of the collimators, therefore mitigating the possible impedance-driven instabilities for the HL-LHC. Figure III.6.27 shows, on the left, the variation of  $Q_0$  versus resistivity for different calibration materials and Mo-coated samples, accounting for different coating sputtering techniques. On the right side, the resistivity of Mo is shown to be in line with expectation for the complete coating production.

The roughness effect can be important in the GHz range, especially when measuring thin conducting layers. Different analytical and numerical models allow to treat the contribution of the roughness as an additional equivalent resistivity. An accurate estimation can be done using the gradient model [39] in which the conductivity is assumed to change proportionally to the bearing contact area. The latter is

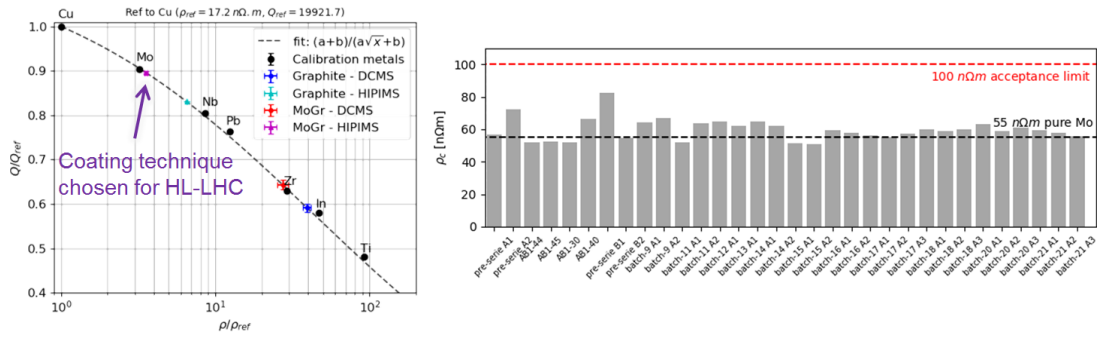


**Fig. III.6.27:** On the left, the variation of  $Q_0$  versus resistivity for different calibration materials and Mo-coated samples. On the right, measured Mo resistivity versus batch production number.

modelled as a function of the RMS roughness,  $R_q$ , measured with optical or mechanical methods.

Figure III.6.28 shows, on the left, the Scanning-Electron Microscope (SEM) images of a Mo coating on MoGr substrate: one can appreciate how the surface characteristics reflect the granular structure of the coating. When accounting for the roughness profile, it is possible to bridge low-frequency measurements to high-frequency ones. This is shown on the right side of Fig. III.6.28: the resistivity obtained with the ECT, once corrected for the roughness effect, matches nicely that obtained directly at the GHz with the H011 cavity.

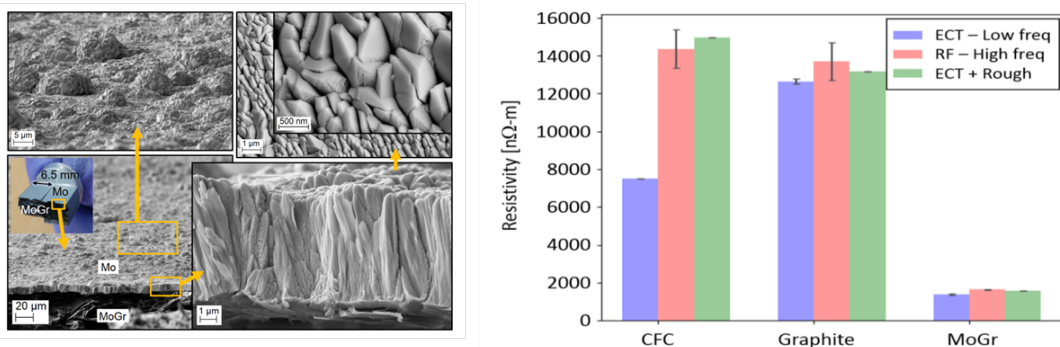


**Fig. III.6.28:** On the left, SEM images of a Mo coating on MoGr substrate. On the right, ECT measurements, with and without roughness correction, compared to the H011 cavity ones.

For higher frequency, e.g. the sub-THz typically achieved by short bunches in synchrotron light sources, the determination of resistivity requires a rather special setup. Optical methods can be applied to study the attenuation in waveguides holding the sample under test [40, 41]. The comparison with analytical models or numerical simulations then allows to obtain the sample resistivity.

### III.6.3.2 Measurement of permittivity

The relative permittivity  $\epsilon_r = \epsilon' - j\epsilon''$  can be measured through resonator measurements [42].

The measurements can be performed by measuring the TE<sub>10n</sub> modes of an empty rectangular cavity connected to a VNA and by measuring the same cavity perturbed by the sample material.

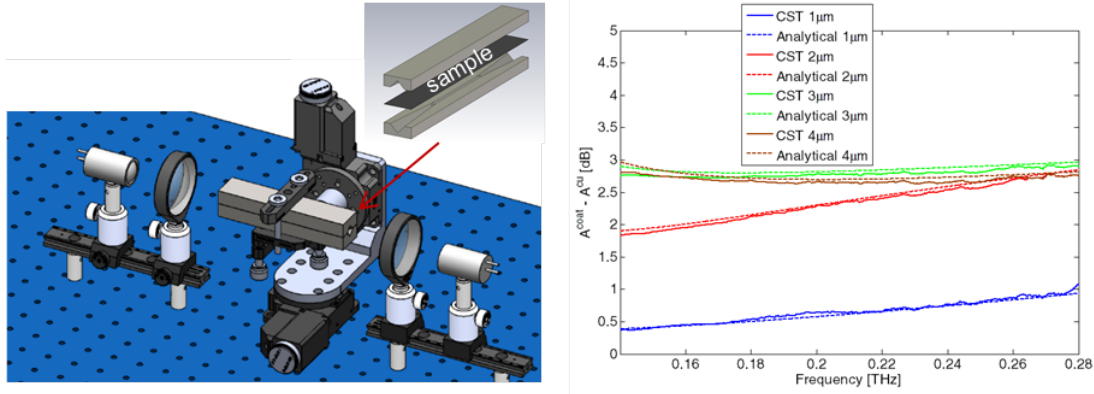


**Fig. III.6.29:** On the left, optical setup for resistivity measurements at THz frequency with exploded view of the sample and holders, on the right, dependence of the attenuation versus frequency for different materials obtained with analytical formulas (dashed line) and numerical frequency domain simulations (full line). Courtesy of A. Passarelli.

By evaluating the changes in mode resonant frequency  $f_r$  and quality factor  $Q_0$  when the sample is inserted into the cavity, permittivity values can be evaluated using the expressions:

$$\epsilon' = 1 + \frac{V_c}{4V_s} \left( \frac{f_{r,e}^2}{f_{r,p}^2} - 1 \right), \quad (\text{III.6.17})$$

$$\epsilon'' = \frac{V_c}{4V_s} \frac{f_{r,e}^2}{f_{r,p}^2} \left( \frac{1}{Q_{0,p}} - \frac{1}{Q_{0,e}} \right), \quad (\text{III.6.18})$$

where “ $e$ ” and “ $p$ ” denote respectively parameters related to the absence and presence of the sample in the cavity, and  $V_c$  and  $V_s$  are the volumes of the cavity and sample, respectively. This method, analogously to the H011 cavity used for conductivity measurements, allows to measure the permittivity at specific frequencies related to the resonator dimensions.

An example of the method application is given in Ref. [43], where a sample of crystal used for channelling high-amplitude particles in particle accelerators was measured. The crystal was inserted at the center of a rectangular resonator, changing its transverse position. Figure III.6.30, on the right, shows the effect on the first TE<sub>01n</sub> modes of the cavity. As one can see, only odd resonances are affected by the sample, for which the electric field is maximum at the sample location. On the left, the extrapolation of permittivity is performed to lower frequencies and used for numerical impedance simulations of a complete crystal-collimator assembly.

Analogously to the case of measurements performed with a H011 cavity, resonator devices inherently provide measurements at discrete frequencies, typically in the GHz range. Open coaxial-probe measurements can cover the frequency ranges between 100 MHz to 10 GHz, while capacitor measurements with an LCR-meter can typically cover from 10 Hz to few MHz. Quasi-optical measurement systems can also be applied for measuring dielectric properties at the sub-THz range [44].

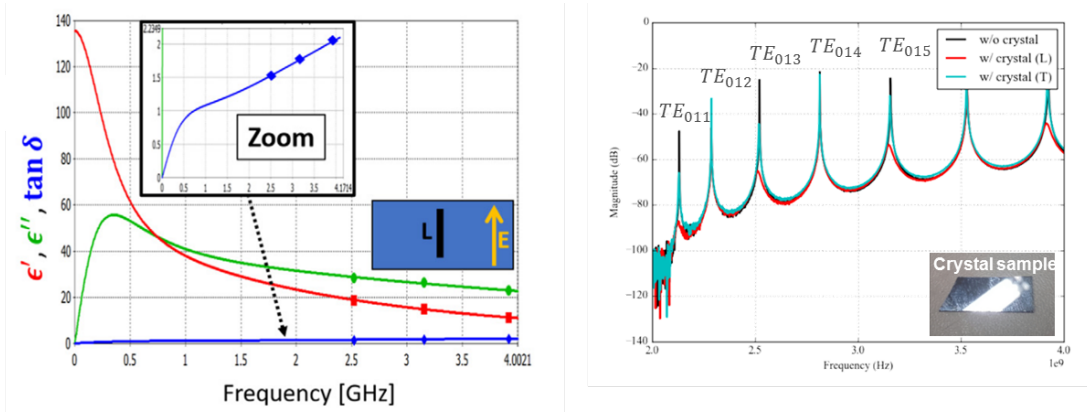


**Fig. III.6.30:** On the right, TE modes of a rectangular resonator in different conditions (no sample inserted, sample parallel (L) or perpendicular (T) to the electric field lines). On the left, extrapolation of the complex permittivity to lower frequencies for numerical impedance simulations.

### III.6.3.3 Measurement of permeability

To complement the resonator-based method described for the determination of the relative permittivity, here we present a method for the determination of the relative permeability  $\mu_r = \mu' - j\mu''$  based on reflection measurements.

The sample holder shown on the left of Fig. III.6.31 is made by cascaded transitions from an N-type connection to the size of the ferrite ring under test. The reflection coefficient  $S_{11}(\mu_r)$  can be computed analytically for each section of the holder, including the ferrite ring. With this setup, the permeability can be typically determined between 1 and 100 MHz [45]. Placing the setup in a dipole, one can study the ferrite under a bias field (e.g., for ferrites used in tunable cavities) as shown in Fig. III.6.31 on the right.

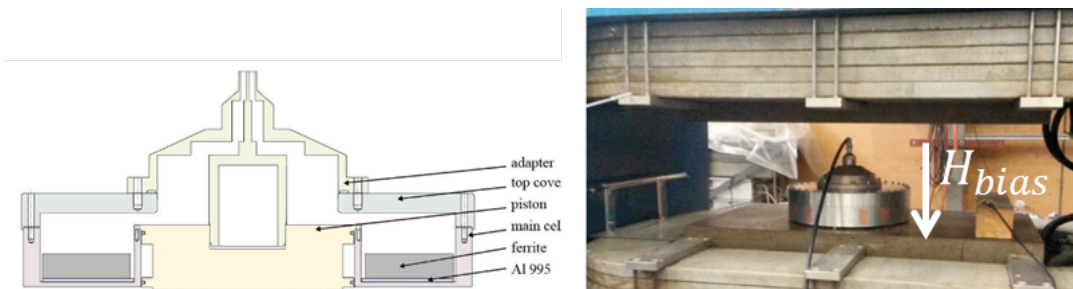


**Fig. III.6.31:** On the left, setup for permeability measurements in reflection. On the right, setup in a dipole bias field. Courtesy of J. Eberhardt.

Figure III.6.32 shows the results of this type of measurement in which  $\mu'$  and  $\mu''$  are determined as a function of frequency and for different bias fields.

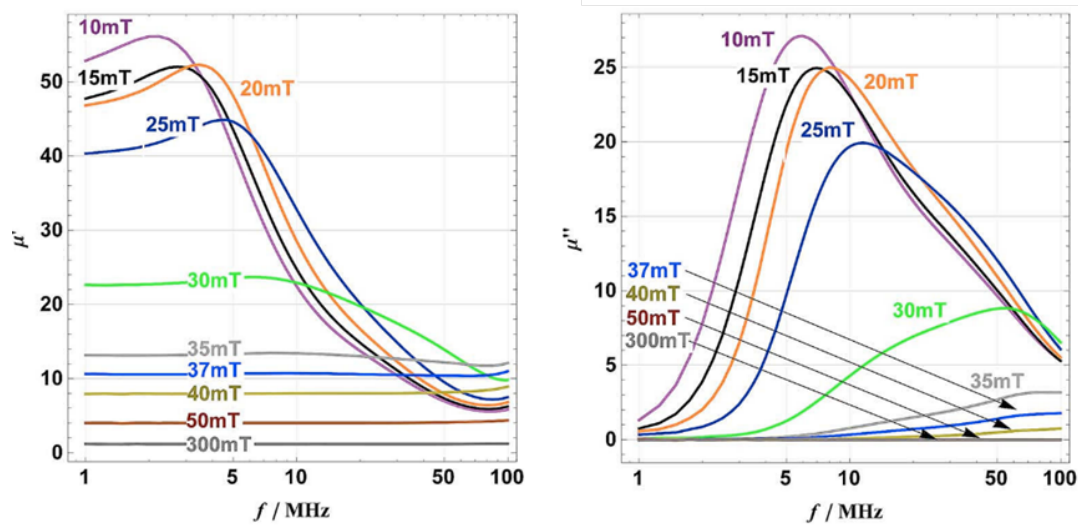


**Fig. III.6.32:** Relative permeability measurement results as a function of frequency and for different bias fields. Courtesy of J. Eberhardt.

### III.6.4 Summary

In this chapter we described beam-based impedance measurements and bench impedance measurements commonly performed in accelerator laboratories. The knowledge of the impedance is crucial for the accurate development of a machine impedance model capable to predict possible beam instabilities under operation conditions and future upgrades.

We also presented common techniques for the electromagnetic characterization of material resistivity, permittivity and permeability, which are essential input for numerical simulations and design of accelerator components.

## References

- [1] L. Palumbo, V. G. Vaccaro, and M. Zobov, Wake fields and impedance, CERN-95-06, CERN, Geneva, Switzerland, 1995, pp. 331, [doi:10.5170/CERN-1995-006.331](https://doi.org/10.5170/CERN-1995-006.331).
- [2] A. W. Chao, Physics of collective beam instabilities in high energy accelerators, Wiley-VCH, New York, 1993, <https://www.slac.stanford.edu/~achao/wileybook.html>.
- [3] K. Ng, Physics of intensity dependent beam instabilities, World Scientific, Singapore, 2002, [doi:10.1142/5835](https://doi.org/10.1142/5835).
- [4] N. Mounet, DELPHI: an analytic Vlasov solver for impedance-driven modes, CERN, Geneva, Switzerland, May 2014, <https://cds.cern.ch/record/1954277>.
- [5] C. Zannini, H. Bartosik, G. Iadarola, G. Rumolo, and B. Salvant, Benchmarking the CERN-SPS transverse impedance model with measured headtail growth rates, CERN-ACC-2015-335, 2015, <https://cds.cern.ch/record/2141779>.
- [6] D. Amorim, PhD thesis, Study of the transverse mode coupling instability in the CERN Large Hadron Collider, 2019, <https://cds.cern.ch/record/2707064>.
- [7] S. Persichelli, M. Migliorati, N. Biancacci, S. Gilardoni, E. Métral, *et al.*, Transverse beam coupling impedance of the CERN Proton Synchrotron, Phys. Rev. Accel. Beams, 19, 041001, 2016, [doi:10.1103/PhysRevAccelBeams.19.041001](https://doi.org/10.1103/PhysRevAccelBeams.19.041001).
- [8] C. Zannini, PhD thesis, Electromagnetic simulation of CERN accelerator components and experimental applications, 2013, <https://cds.cern.ch/record/1561199>.
- [9] N. Biancacci, Impedance localization and identification, ICFA mini-Workshop on Mitigation of Coherent Beam Instabilities in Particle Accelerators (MCBI 2019), Zermatt, Switzerland, 23–27 Sep 2019, pp. 141, [doi:10.23732/CYRCP-2020-009.141](https://doi.org/10.23732/CYRCP-2020-009.141).
- [10] N. Biancacci, Beam coupling impedance localization technique validation and measurements in the CERN machines, Proc. 4th International Particle Accelerator Conference, Shanghai, China, 2013, <https://cds.cern.ch/record/1578579>.
- [11] N. Biancacci, PhD thesis, Improved techniques of impedance calculation and localization in particle accelerators, 2014, <https://cds.cern.ch/record/1704527>.
- [12] L. Emery, G. Decker and J. Galayda, Local bump method for measurement of transverse impedance of narrow-gap ID chambers in storage rings, Proc. of 2001 Particle Accelerator Conference, Chicago, Illinois U.S.A., June 18-22, 2001, [doi:10.1109/PAC.2001.987195](https://doi.org/10.1109/PAC.2001.987195).
- [13] V. Smaluk, X. Yang, A. Blednykh, Y. Tian and K. Ha, AC orbit bump method of local impedance measurement, Nuclear Inst. and Methods in Physics Research, A 871 (2017) 59–62, [doi:10.1016/j.nima.2017.07.067](https://doi.org/10.1016/j.nima.2017.07.067).
- [14] S. A. Antipov, C. Accettura, D. Amorim, A. Bertarelli, N. Biancacci, *et al.*, Transverse beam stability with low-impedance collimators in the High-Luminosity Large Hadron Collider: Status and challenges, Phys. Rev. Accel. Beams, 23, 034403, 2020, [doi:10.1103/PhysRevAccelBeams.23.034403](https://doi.org/10.1103/PhysRevAccelBeams.23.034403).

- [15] M. Migliorati, S. Persichelli, L. Ventura, N. Biancacci, H. Damerau, *et al.*, Measurements of the CERN PS longitudinal resistive coupling impedance, Proc. IPAC2016, Busan, Korea, 2016, pp. 626, [doi:10.18429/JACoW-IPAC2016-MOPOR014](https://doi.org/10.18429/JACoW-IPAC2016-MOPOR014).
- [16] J. L. Laclare, Proc. CAS 1985, CERN, Geneva, Switzerland, 1987, pp. 264–326, [doi:10.5170/CERN-1987-003-V-1.264](https://doi.org/10.5170/CERN-1987-003-V-1.264).
- [17] A. Lasheen and E. Shaposhnikova, Evaluation of the CERN Super Proton Synchrotron longitudinal impedance from measurements of the quadrupole frequency shift, Phys. Rev. Accel. Beams, 20, 064401, 2017, [doi:10.1103/PhysRevAccelBeams.20.064401](https://doi.org/10.1103/PhysRevAccelBeams.20.064401).
- [18] S. A. Antipov, D. Amorim, N. Biancacci, X. Buffat, E. Métral, *et al.*, Proof-of-Principle Direct Measurement of Landau Damping Strength at the Large Hadron Collider with an Antidamper, Phys. Rev. Lett. 126, 164801, 2021, [doi:10.1103/PhysRevLett.126.164801](https://doi.org/10.1103/PhysRevLett.126.164801).
- [19] N. Biancacci and R. Tomás, Using ac dipoles to localize sources of beam coupling impedance, Phys. Rev. Accel. Beams 19, 054001, 2016, [doi:10.1103/PhysRevAccelBeams.19.054001](https://doi.org/10.1103/PhysRevAccelBeams.19.054001).
- [20] D. Boussard, Schottky noise and beam transfer function diagnostics, CAS - CERN Accelerator School : 5th Advanced Accelerator Physics Course, pp.749–782, 1995, [doi:10.5170/CERN-1995-006.749](https://doi.org/10.5170/CERN-1995-006.749).
- [21] N. Biancacci and M. Zampetakis, Simulation and measurement of the interplay between electron cooling, impedance, intrabeam scattering, and space charge for coasting beams, Phys. Rev. Accel. Beams 27, 014201 2024, [doi:10.1103/PhysRevAccelBeams.27.014201](https://doi.org/10.1103/PhysRevAccelBeams.27.014201).
- [22] O. Brüning, P. Collier, P. Lebrun, S. Myers, R. Ostojic, *et al.* eds., LHC design report, CERN, Geneva, Switzerland, 2004, [doi:10.5170/CERN-2004-003-V-1](https://doi.org/10.5170/CERN-2004-003-V-1).
- [23] A. Mostacci and F. Caspers, History and development of bench measurement techniques for impedance evaluation, Electromagnetic wake fields and impedances in particle accelerators, Erice, 24–28 April 2014, <https://indico.cern.ch/event/287930/>
- [24] M. Sands and J. Rees, A bench measurement of the energy loss of a stored beam to a cavity, SLAC Report PEP-95, 8 August 1974, <https://cds.cern.ch/record/894800>.
- [25] M. Paniello, V. G. Vaccaro, R. Masullo, The stretched wire method: A comparative analysis performed by means of the mode matching technique, Proc. 25th International Linear Accelerator Conference, LINAC10, Tsukuba, Japan, September 12–17, 2010, <https://accelconf.web.cern.ch/LINAC2010/papers/thp081.pdf>.
- [26] H. Hahn and F. Pedersen, On coaxial wire measurements of the longitudinal coupling impedance, BNL Rep. 50860, 1978, [doi:10.2172/6591101](https://doi.org/10.2172/6591101).
- [27] L. S. Walling, D. E. McMurry, D. V. Neuffer and H. A. Thiessen, Transmission-line impedance measurements for an advanced hadron facility, Nucl. Instrum. Meth. A, 281, 1989, pp. 433–447, [doi:10.1016/0168-9002\(89\)91474-5](https://doi.org/10.1016/0168-9002(89)91474-5).
- [28] V. G. Vaccaro, Coupling impedance measurements: an improved wire method, INFN TC-94/023, 1994, <https://cds.cern.ch/record/276443>.
- [29] B. Spataro, D. Brandt, F. Caspers, D. Li, M. Migliorati, *et al.*, On trapped modes in the LHC recombination chambers: numerical and experimental results, Nucl. Instrum. Meth. A, 517, 2004, pp. 19–27, [doi:10.1016/j.nima.2003.09.046](https://doi.org/10.1016/j.nima.2003.09.046).

- [30] N. Biancacci, F. Caspers, J. Kuczerowski, E. Métral, N. Mounet, *et al.*, “Impedance simulations and measurements on the LHC collimators with embedded beam position monitors”, PRAB 20, 011003 (2017), [doi:10.1103/PhysRevAccelBeams.20.011003](https://doi.org/10.1103/PhysRevAccelBeams.20.011003).
- [31] N. Biancacci, F. Caspers, I. Lamas Garcia, A. Grudiev, J. Kuczerowski, *et al.*, Impedance Measurements and Simulations on the TCTP and TDI LHC Collimators, Proceedings of IPAC2016, Busan, Korea, 2016, [doi:10.18429/JACoW-IPAC2016-MOPOR010](https://doi.org/10.18429/JACoW-IPAC2016-MOPOR010).
- [32] T. Kroyer, F. Caspers, and E. Gaxiola, Longitudinal and Transverse Wire Measurements for the Evaluation of Impedance Reduction Measures on the MKE Extraction Kickers, CERN AB-Note-2007-028, Geneva, Switzerland, 2007, <http://cds.cern.ch/record/1035461>.
- [33] J. C. Slater, Microwave Electronics, D. Van Nostrand Co., Inc., 1950.
- [34] M. B. Heaney, Electrical Measurement, Signal Processing, and Displays; CRC Press: Boca Raton, FL, USA, 2003.
- [35] Eddy Current Testing. In NDE Handbook; Bøving, K.G. (Ed.) Butterworths: London, UK, 1989; Chapter 5; pp. 42–59, [doi:10.1016/B978-0-408-04392-2.50011-4](https://doi.org/10.1016/B978-0-408-04392-2.50011-4).
- [36] J. W. Luquire, W. E. Deeds and C. V. Dodd, Alternating Current Distribution Between Planar Conductors, J. Appl. Phys. 1970, 41, 3983–3991, [doi:10.1063/1.1658399](https://doi.org/10.1063/1.1658399).
- [37] C. Accettura, D. Amorim, S. A. Antipov, A. Baris, A. Bertarelli, N. Biancacci, *et al.* Resistivity Characterization of Molybdenum-Coated Graphite-Based Substrates for High-Luminosity LHC Collimators, Coatings 2020, 10, 361, [doi:10.3390/coatings10040361](https://doi.org/10.3390/coatings10040361).
- [38] M. Juillard, B. Aune, B. Bonin and L. Wartski, Superconducting Surface Resistance Measurements with a TE011 Cavity, in proceedings of the 2nd European Particle Accelerator Conference, Nice, France, 12–16 June 1990, pp. 1106–1108, <https://cds.cern.ch/record/963960>
- [39] G. Gold, K. Helmreich, A Physical Surface Roughness Model and Its Applications, IEEE Trans. Microw. Theory Tech. 2017, 65, 3720–3732, [doi:10.1109/TMTT.2017.2695192](https://doi.org/10.1109/TMTT.2017.2695192).
- [40] A. Passarelli, H. Bartosik, G. Rumolo, V. G. Vaccaro, M. R. Masullo, *et al.*, Novel measurement technique for the electromagnetic characterization of coating materials in the sub-THz frequency range, Phys. Rev. Accel. Beams, vol. 21, issue 10, Oct. 2018, <https://journals.aps.org/prab/pdf/10.1103/PhysRevAccelBeams.21.103101>.
- [41] A. Passarelli, C. Koral, M. R. Masullo, W. Vollenberg, L. L. Amador, *et al.*, Sub-THz Waveguide Spectroscopy of Coating Materials for Particle Accelerators, Condens. Matter 2020, 5, 9, [doi:10.3390/condmat5010009](https://doi.org/10.3390/condmat5010009).
- [42] V. R. K. Murthy and R. Raman, A method for the evaluation of microwave dielectric and magnetic parameters using rectangular cavity perturbation technique, Solid State Communications, Vol. 70, No. 8, pp. 847-850, 1989, [doi:10.1016/0038-1098\(89\)90510-3](https://doi.org/10.1016/0038-1098(89)90510-3).
- [43] D. Quartullo, P. Arpaia, N. Biancacci, F. Giordano, I. Llamas Garcia, *et al.*, Electromagnetic characterization of the crystal primary collimators for the HL-LHC, Nucl. Instrum. Meth. A 1010 (2021), 165465, [doi:10.1016/j.nima.2021.165465](https://doi.org/10.1016/j.nima.2021.165465).
- [44] L. F. Chen, C. K. Ong, C. P. Neo, V. V. Varadan, V. K. Varadan, Microwave Electronics: Measurement and Materials Characterization, John Wiley & Sons, Ltd, 2004.

- [45] J. Eberhardt, F. Caspers and C. Vollinger, Ferrite characterization for the design of an accelerating cavity with perpendicular biasing, IEEE TNS, 63, 2, 2016, [doi:10.1109/TNS.2015.2463091](https://doi.org/10.1109/TNS.2015.2463091).